

---

This is an electronic reprint of the original article.  
This reprint may differ from the original in pagination and typographic detail.

Ghaderzadeh, Sadegh; Ghorbani-Asl, Mahdi; Kretschmer, Silvan; Hlawacek, Gregor; Krasheninnikov, Arkady V.

## Channeling effects in gold nanoclusters under He ion irradiation

*Published in:*  
Nanotechnology

*DOI:*  
[10.1088/1361-6528/ab4847](https://doi.org/10.1088/1361-6528/ab4847)

Published: 17/01/2020

*Document Version*  
Publisher's PDF, also known as Version of record

*Published under the following license:*  
CC BY

*Please cite the original version:*  
Ghaderzadeh, S., Ghorbani-Asl, M., Kretschmer, S., Hlawacek, G., & Krasheninnikov, A. V. (2020). Channeling effects in gold nanoclusters under He ion irradiation: Insights from molecular dynamics simulations. *Nanotechnology*, 31(3), 1-11. Article 035302. <https://doi.org/10.1088/1361-6528/ab4847>

---

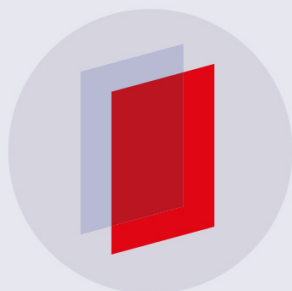
This material is protected by copyright and other intellectual property rights, and duplication or sale of all or part of any of the repository collections is not permitted, except that material may be duplicated by you for your research use or educational purposes in electronic or print form. You must obtain permission for any other use. Electronic or print copies may not be offered, whether for sale or otherwise to anyone who is not an authorised user.

PAPER • OPEN ACCESS

## Channeling effects in gold nanoclusters under He ion irradiation: insights from molecular dynamics simulations

To cite this article: Sadegh Ghaderzadeh *et al* 2020 *Nanotechnology* **31** 035302

View the [article online](#) for updates and enhancements.



**IOP | ebooks™**

Bringing you innovative digital publishing with leading voices to create your essential collection of books in STEM research.

Start exploring the collection - download the first chapter of every title for free.

# Channeling effects in gold nanoclusters under He ion irradiation: insights from molecular dynamics simulations

Sadegh Ghaderzadeh<sup>1,3</sup> , Mahdi Ghorbani-Asl<sup>1</sup> , Silvan Kretschmer<sup>1</sup> , Gregor Hlawacek<sup>1</sup>  and Arkady V Krasheninnikov<sup>1,2</sup> 

<sup>1</sup>Institute of Ion Beam Physics and Materials Research, Helmholtz-Zentrum Dresden-Rossendorf, D-01314 Dresden, Germany

<sup>2</sup>Department of Applied Physics, Aalto University School of Science, PO Box 11100, FI-00076 Aalto, Finland

E-mail: [s.ghaderzadeh@hzdr.de](mailto:s.ghaderzadeh@hzdr.de) and [a.krasheninnikov@hzdr.de](mailto:a.krasheninnikov@hzdr.de)

Received 18 April 2019, revised 22 August 2019

Accepted for publication 26 September 2019

Published 17 October 2019



## Abstract

The interpretation of helium ion microscopy (HIM) images of crystalline metal clusters requires microscopic understanding of the effects of He ion irradiation on the system, including energy deposition and associated heating, as well as channeling patterns. While channeling in bulk metals has been studied at length, there is no quantitative data for small clusters. We carry out molecular dynamics simulations to investigate the behavior of gold nanoparticles with diameters of 5–15 nm under 30 keV He ion irradiation. We show that impacts of the ions can give rise to substantial heating of the clusters through deposition of energy into electronic degrees of freedom, but it does not affect channeling, as clusters cool down between consecutive impact of the ions under typical imaging conditions. At the same time, high temperatures and small cluster sizes should give rise to fast annealing of defects so that the system remains crystalline. Our results show that ion-channeling occurs not only in the principal low-index, but also in the intermediate directions. The strengths of different channels are specified, and their correlations with sputtering-yield and damage production is discussed, along with size-dependence of these properties. The effects of planar defects, such as stacking faults on channeling were also investigated. Finally, we discuss the implications of our results for the analysis of HIM images of metal clusters.

Keywords: helium ion microscope, ion irradiation, sputtering-yield, channeling, gold nanostructures

(Some figures may appear in colour only in the online journal)

## 1. Introduction

As compared to their bulk counterparts, nano-objects, such as atomic clusters, and nanostructured materials possess unique

properties related to size-quantization effects [1, 2] and high surface-to-volume ratio. This provides vast opportunities for tuning their optical and electronic properties for a wide range of applications, including optoelectronics and catalysis, through only changing the system size [3, 4].

The properties of nanomaterials can further be tailored by beams of energetic particles, such as electrons or ions, see [5–7] for an overview. Ion irradiation and implantation, which are routinely used nowadays in the semiconductor industry, work particularly well in this case, as system size is comparable to or less than the typical ion range of ions in the

<sup>3</sup> Author to whom any correspondence should be addressed.

commercially available accelerators, so that the whole system can easily be treated by the beam.

At the same time, low-dimensional systems, such as clusters or sheets of graphene or transition metal dichalcogenides do not behave as bulk materials under irradiation, as numerous experiments and simulations indicate [8–14]. Due to a small system size with respect to ion ranges in the corresponding bulk material, only a part of ion energy can be adsorbed by the target, so that the cross section for defect production decreases with increasing ion energy. The evolution of the target structure under ion irradiation can also be different due to high forward and sideward sputtering rates, reduction or absence of collisional cascades and longer lifetimes of electronic excitations in the target.

For crystalline nanosystems, interaction of the ions with the target will also be affected by its orientation with respect to the incident ion beam direction, the so called channeling effects, when ions move between the rows of atoms and consequently penetrate much deeper and lose less energy [15, 16]. Although this phenomenon is well-understood for bulk systems [15–19], channeling may be different in nanosystems, and specifically metallic clusters, due to surface reconstructions, different annealing rates of point defects and beam heating of small clusters with a limited heat transfer to the environment.

An additional motivation to study channeling, that is the effects of cluster orientation with respect to the incident beam direction, is helium ion microscopy (HIM) [20–22], a modern tool based on a gas field ionization source. HIM can provide valuable information on the morphology, composition and structure of nanoparticles, which it is critical for their efficient application and also to address toxicological questions related to the increased use of nanoparticles in consumer products, medicine and nutrition [23, 24]. HIM is employed for imaging as well as patterning of conductive and insulating materials at the nano-scale [20, 25–27]. The orientation of the crystalline targets should be accounted for in the interpretation of HIM or focused ion beam (FIB) images [28]. In particular, channeling can increase the final image contrast by a factor of two [29, 30] and might be used to obtain information on the crystal orientation of the target [29, 31]. This contrast between channeling and non-channeling conditions can be utilized to reveal details about the atomistic structure of the sample [32].

To achieve this aim, a comprehensive description of the irradiation process in HIM is required, which is the main scope of our study. To this end, several questions arise: How do small metal clusters behave under He irradiation for typical ion energies (30 keV) used in HIM? Does channeling occur in systems where surface atom reconstructions take place or that contain extended 2D defects such as stacking faults, and if so what are channeling and non-channeling directions, and what is the difference? Will channeling be affected by beam-induced heating? Are such behaviors size-dependent?

Molecular dynamics (MD) studies on gold nanoparticles under heavy ion irradiation (such as Au ions/clusters, Ga and Ar) have been reported [33–38], and MD simulations [39] of He ion irradiations of silicon and tungsten crystals have been

carried out in the context of channeling contrast simulations of HIM images. However, none of these studies have considered light ion irradiation (e.g. He ions) of gold nanoclusters. At the same time, it is well known that the behavior of the target under light ion irradiation is different from that under heavy ion bombardment [40–44].

In the present study, we perform empirical potential MD simulations to investigate freestanding gold nanoclusters of different sizes under 30 keV He ion irradiation to address the above-mentioned issues and get insights into ion-target interaction in HIM and to provide the data required to interpret the experimental HIM images. As channeling maps for nanoclusters obviously cannot be obtained from ion depth profile as the target dimensions are smaller than the typical ion range, we instead derive these maps via ion energy-loss calculations. Our results show that ion-channeling in small systems occurs not only in the principal low-index directions, but also in the intermediate ones. The strengths of different channels are specified, and their correlations with sputtering-yield and damage production are discussed. Channeling patterns are correlated with the intrinsic structural symmetries and the influence of 2D defects on the final channeling pattern is studied. Finally the size-dependence of the results is addressed.

## 2. Method

Empirical potential MD simulations using the LAMMPS computational package [45] were performed as detailed below.

### 2.1. Interatomic potentials

To describe interaction between Au atoms, we employed an embedded-atom method (EAM) potential [46]. As the separations between the atoms and ions can be very small in high-energy collisions, and because ‘standard’ potentials may not be accurate at small inter-atomic distances, the EAM potential was splined to the Ziegler–Biersack–Littmark [47] universal potential and test calculations were made. The results for channeling effect studies were essentially the same, indicating that the EAM potential is well suited for describing ion-target atom collisions.

### 2.2. Electronic stopping

The slowing down process of energetic particles into matter is traditionally separated into elastic collisions with target nuclei and inelastic interactions with electrons, which gives rise to electronic excitations in the target. The electronic stopping power for light He ions with keV energies is always dominant over nuclear stopping contribution. Nevertheless, as we show below, the *direct* effects of electronic stopping on ion channeling pattern is negligible for small clusters, as the ion loses only a few percent of its kinetic energy.

At the same time, the deposited energy is converted to heat, which may *indirectly* affect the behavior of clusters

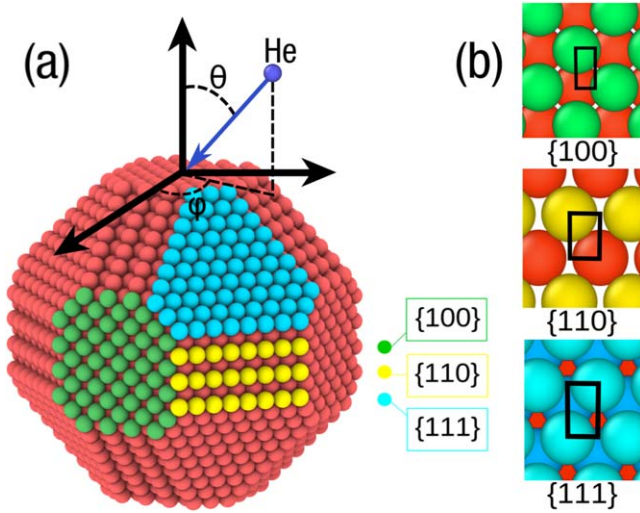


**Figure 1.** (a) Atomistic structure of a gold nano-cluster with a diameter of 5 nm. High symmetry faces and incident ion angles are shown. (b) Irreducible areas used in the ion impact simulations on {100}, {110}, and {111} surfaces.

under irradiation and the channeling pattern. The typical time scale for the impinging ions to go through the target is of the order of femtosecond, while the typical time scale for electron-phonon energy exchange is in the picosecond range. Consequently, the energy deposited by the ion through electronic stopping should not affect the propagation (i.e. direction) of that ion through the system and thus the related channeling effects. However, the deposited energy may give rise to heating or even melting of a small cluster, which may influence defect annealing and, potentially, if the beam current is high enough, the propagation of the next ion through the system. Considering this, we carefully analyzed possible size-dependent heating of the clusters.

### 2.3. Analysis of atomic configurations after ion impacts

Distortions from pristine configuration can be detected through the calculations of the centrosymmetry parameter [48]. In this approach, the parameter is zero for the perfect structure and increases for higher displacements of the substrate atoms. This is an appropriate tool to recognize and analyze defects in a distorted structure in a systematic way [49].

### 2.4. Simulation setup

Freestanding gold nanoclusters of 5, 10 and 15 nm sizes in diameter, containing 4501, 35325 and 118293 gold atoms respectively, were constructed using the Wulff method, where each cluster is terminated by the three main faces ({100}, {110} and {111}) (figure 1). The Wulff structures studied in this work were optimized using the above-mentioned interatomic potential before any channeling simulations. Given that the potential is well tested and the results obtained using that potential were found to be in agreement with the experimental data, especially for surfaces and surface reconstructions [46], one can expect that the structures we considered

represent well the experimental clusters. The energy of He ions was chosen to be 30 keV, the typical ion energy in HIM.

Taking an appropriate irreducible area, the impacts of energetic He ions into the clusters were simulated. In order to collect enough statistics, 1000 simulations per irreducible area, for every pair of incident polar and azimuthal angles ( $\theta_0$  and  $\phi_0$ , respectively), were performed as shown in figure 1. An adaptive time-step method for impact simulations has been used as implemented in LAMMPS.

## 3. Results and discussions

### 3.1. Electronic stopping and heating of the clusters

The average energy  $E_{dep}$  lost by the impinging ion passing through a spherical cluster of radius  $R$  is

$$E_{dep} = \frac{4}{3}S_e R, \quad (1)$$

where  $S_e$  is the electronic stopping power.

Assuming that all deposited energy remains in the system and is not carried away by the emitted energetic electrons or sputtered atoms, the total additional kinetic energy  $E_{kin}$  of the atoms in the cluster is

$$E_{kin} = \frac{1}{2}E_{dep}, \quad (2)$$

where the factor 1/2 is added due to the equipartition theorem and accounts for the potential energy degrees of freedom.

At the same time, for a cluster composed from  $N$  atoms in thermal equilibrium

$$E_{kin} = \frac{3}{2}k_B T N, \quad (3)$$

where  $k_B$  is the Boltzmann constant and  $T$  is the temperature of the system.

The temperature increase  $\Delta T$  can then be expressed as

$$\Delta T = \left( \frac{1}{3k_B \pi \rho} \right) \frac{S_e}{R^2} \times \alpha, \quad (4)$$

where  $\rho$  is the density of the cluster material (assumed to be the same as in bulk gold), and the scaling factor  $\alpha$ ;  $0 < \alpha < 1$  was introduced to account for energy dissipation into the environment. We stress that energy conversion from the electronic degrees of freedom into phonons should be very efficient in metallic systems, so that one can expect that little energy will be dissipated into the environment through thermal conductance and black body radiation before the cluster reaches the thermodynamic equilibrium.

Assuming that the cluster was at room temperature  $T_0 = 300$  K before the impact, and  $T = T_0 + \Delta T$  after the impact, by using equation (4) and the data on  $S_e$  provided by SRIM [50], one can estimate  $T$  after the impact of the ion and compare it to the melting point of Au clusters. In figure 2 the results of our calculations for typical He ion energies and the experimental data taken from [51] are shown.

It is evident that irradiation can substantially increase  $T$ , but for the He ion energy considered (30 keV,

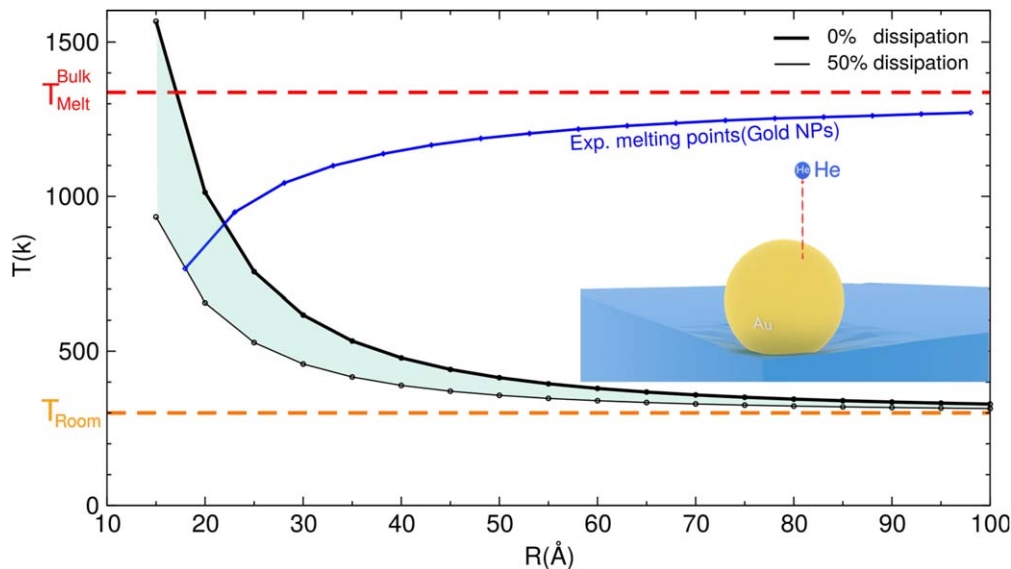


**Figure 2.** Maximum increase in temperature of Au clusters induced by the energy deposited by a 30 keV He ion through electronic stopping as a function of cluster radius. Experimental data on melting temperature of Au clusters [51] is presented as well. Temperature increase was evaluated assuming no dissipation and dissipation of 50% of heat into the environment through thermal conductance and black body radiation.

$S_e = 16.21 \text{ eV } \text{\AA}^{-1}$ ) and without any energy dissipation ( $\alpha = 1$ ), even the smallest considered clusters will remain crystalline. Moreover, high temperatures indicate that annealing of point and extended defects will be very efficient due to their migration and annihilation at the cluster surfaces. At the same time, for the typical current used in HIM of about 1 pA and a pixel size of  $1 \times 1 \text{ nm}$ , the characteristic time between collisions of ions with clusters of few nanometers in diameters are of the order of tens of nanoseconds, which is at least two orders of magnitude longer than the typical time  $t_c \sim$  of cooling the clusters through heat dissipation into the substrate. This time scale can be estimated based on the value of  $410 \text{ MW m}^{-2} \text{ K}^{-1}$  of thermal boundary conductance measured for Au nanoparticles in a polymer matrix [52]. Thus, one can assume that by the time the cluster is being hit by the next He ion, all extra energy brought in by the previous ion is fully dissipated into the environment and most of the defects (at least point defects) have disappeared. Taking this into account, the effects of ion beam heating on propagation of ions in the clusters can be neglected.

### 3.2. Sputtering of target atoms

Due to their very geometry, nanostructured materials are more sensitive to ion irradiation, as sideward and forward sputtering is possible. To this end, although collisions of light energetic He ions with bulk metals composed from heavy atoms such as Au can barely sputter any atoms from the surface and the total sputtering yield is low, for clusters there might be a relatively high sputtering yield depending on the impact point and ion incident angle, which we estimated for freestanding systems.

Ion energy-loss and sputtering yield as functions of incident angle for different incident ion beam directions are shown in figure 3. The correlation between the sputtering

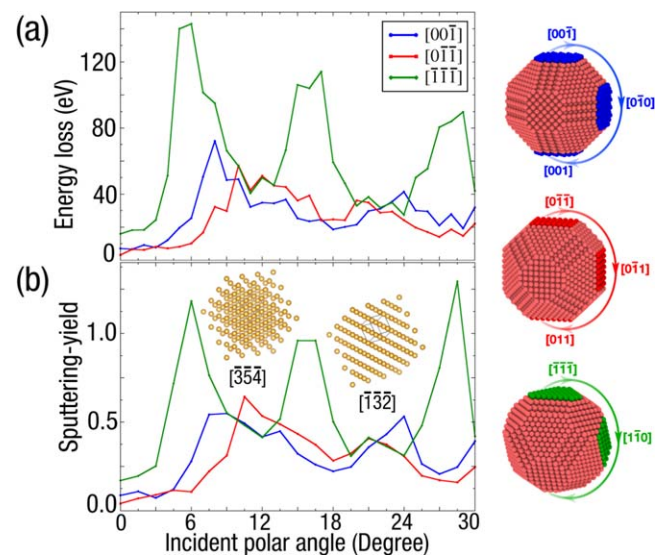


**Figure 3.** (a) Ion energy-loss as a function of incident beam tilt angle for three different starting directions. The inset shows the view on the crystal surface corresponding to the minima observed for the green curve. (b) Sputtering yield as functions of incident polar angle for different ion beam directions. The insets present views along the two remaining starting directions  $[00\bar{1}]$  and  $[0\bar{1}\bar{1}]$ . Incident azimuthal angles are fixed, as shown on the right-hand side.

yield and ion energy loss is evident: the larger the energy-loss, the higher the sputtering yield, which reflects the conservation of the lost energy for each direction. The minima in the curves correspond to different channeling directions. For the green curve in figure 3 with a starting direction of  $[\bar{1}\bar{1}\bar{1}]$  these are with increasing tilt angle the  $[\bar{3}\bar{5}\bar{4}]$  direction at  $11.54^\circ$  and the  $[\bar{1}\bar{3}\bar{2}]$  direction at  $22.21^\circ$ . The corresponding views from the beam on the structure are shown as insets in figure 3(b). While the same applies to the other two presented

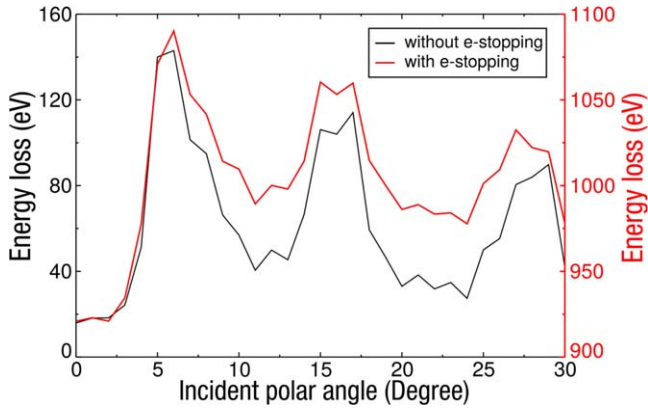


**Figure 4.** A comparison between ion energy-loss with and without account for the electronic stopping for  $[\bar{1}\bar{1}\bar{1}]$  direction.

cases the curves are flatter as the rotation is performed in the  $(\bar{1}00)$  plane which is strong planar channeling configuration.

In order to assess the direct effects of the electronic stopping on the channeling pattern, we also carried out calculations including electronic stopping power  $S_e$  as frictional force with the values matching the experiments (TRIM). It naturally gave rise to higher energy loss (about 3% of the initial total energy), yet the channeling pattern is almost the same, as evident from figure 4. The reason becomes clearer, when one looks at the Lindhards critical channeling angle  $\Psi$  [53]:

$$\Psi = \sqrt{\frac{2Z_1Z_2e^2}{Ed}}, \quad (5)$$

where  $Z_1$  and  $Z_2$  are the charges of the projectile and target atom nuclei,  $E$  is the energy of the incident ion, and  $d$  is the distance between the atoms in the channel. The values of  $\Psi$  before and after the ion loses about 3% of the initial total energy, as detailed in the table 1. This means that the critical channeling angles for [100], [110] and [111] directions change by only 0.03°, 0.05° and 0.03° respectively after the energy loss. Therefore, excluding electronic stopping does not affect channeling patterns.

The analysis of the MD data indicates that the majority of He ions go through the gold clusters without any noticeable deviation from their incident direction, showing an overall linear relation between incident and exit ion angles (see figure 5). However, from the plots in figure 5 one can also observe the ion beam steering into nearby low index channels. Looking at the data for the polar angles in the  $(\bar{1}\bar{1}2)$  plane (green curve) one can see that for polar incident angles from 6° to 15° the exit angle is always around 12° (all angles relative to the  $[1\bar{1}\bar{1}]$  towards  $[1\bar{1}0]$  the in the  $(\bar{1}\bar{1}2)$  plane). The reason for this behavior is the steering of the incoming ion beam into the nearby channel along the  $[\bar{3}\bar{5}\bar{4}]$  direction. The total width of this channel can be estimated from figure 3(a) and matches well with the width of the plateau observed in figure 5.

30 keV He ions do not have enough momentum to generate significant collision cascades near the surface leading to cluster emission, so sputtering in general occurs

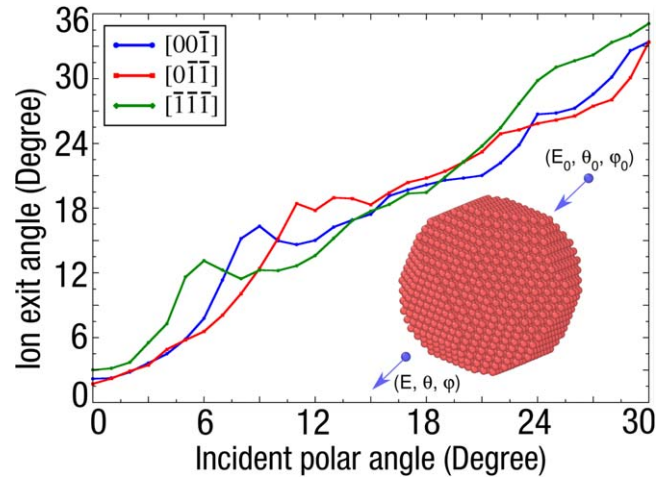


**Figure 5.** Ion exit versus incident polar angles for a 5 nm Au cluster. Incident azimuthal angles are fixed as following: Black:  $[00\bar{1}]$  towards  $[0\bar{1}\bar{1}]$  around  $[\bar{1}00]$ , Red:  $[0\bar{1}\bar{1}]$  towards  $[0\bar{1}0]$  around  $[\bar{1}00]$ , and Green:  $[\bar{1}\bar{1}\bar{1}]$  towards  $[1\bar{1}0]$  around  $[\bar{1}\bar{1}2]$ .

**Table 1.** The critical channeling angles for He ion into a 5 nm gold target. Based on the Lindhard equation.

Directions	[100]	[110]	[111]
30 keV	4.04	5.23	2.67
29 keV	4.07	5.28	2.70

monotonically. The average sputtering-yield we obtain in our calculations is naturally higher than the one obtained experimentally or numerically for surfaces of bulk Au due to forward and sideward sputtering. The reason for this is that also forward sputtering from the bottom and sides of the nanocrystal contributes to total sputter yield. This is evident from the distribution of sputtered atoms for the upper and lower half of the cluster (see figure 6).

### 3.3. Channeling of ions

Channeling effects in bulk materials can be assessed from range of the ions in the target [18, 19]. However, this ion-range approach cannot be used for finite systems, the dimensions of which are smaller than the typical ion range. Therefore we used the ions energy loss, instead of its range, as the criterion. In our simulations, we first kept the azimuthal angle fixed, while the incident polar angle changes from  $-20^\circ$  to  $20^\circ$  (figure 7).

In figures 7(a) and (b) nearby low index channeling directions are marked.

**3.3.1. Energy loss.** For ions with only a small deviation from the directions discussed in figure 7, the ions impinging along the  $(\bar{1}\bar{1}0)$  direction show the lowest ion energy dissipation followed by ions along the  $\langle 00\bar{1} \rangle$  and  $\langle \bar{1}\bar{1}\bar{1} \rangle$  ones. Correspondingly, the lowest damage production and also the lowest sputtering yield in this direction can be expected. One of the conclusions that can be drawn from energy-loss

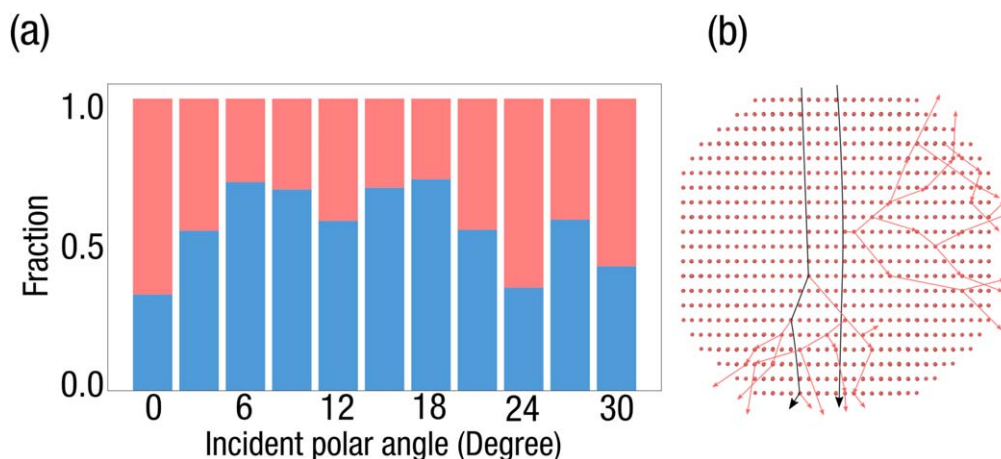


**Figure 6.** Left: (a) relative sputter yield for the sputtered particles into the upper (red) and lower (blue) hemisphere for a 5 nm gold cluster. (The polar angle is measured in the  $[\bar{1}\bar{1}2]$  plane and increases from  $[\bar{1}\bar{1}\bar{1}]$  towards  $[1\bar{1}0]$ .) (b) Typical ion (black lines) and atom (red) trajectories: depending on channeling conditions, cascades can develop upward or downward.

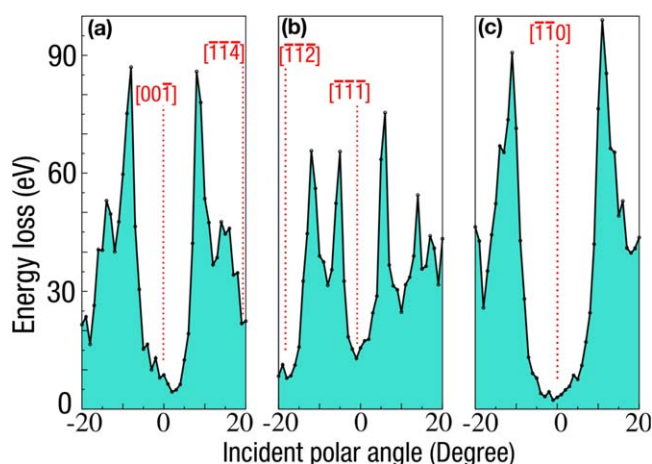


**Figure 7.** Ion energy-loss of a 30 keV He ion in a 5 nm gold cluster for a range from  $-20^\circ$  to  $20^\circ$  polar angle around the (a)  $[00\bar{1}]$  direction tilted towards  $[\bar{1}\bar{1}\bar{1}]$ , (b)  $[\bar{1}\bar{1}\bar{1}]$  direction towards  $[\bar{1}\bar{1}0]$  and (c)  $[\bar{1}\bar{1}0]$  around tilted towards  $[\bar{1}\bar{1}\bar{1}]$ . Incident azimuthal angles are fixed as following: (a)  $[00\bar{1}]$  towards  $[\bar{1}\bar{1}\bar{1}]$ , (b):  $[\bar{1}\bar{1}\bar{1}]$  towards  $[\bar{1}\bar{1}0]$ , and (c):  $[\bar{1}\bar{1}0]$  towards  $[\bar{1}\bar{1}\bar{1}]$ .

patterns is that ion-channeling in clusters occurs not only in the principal low-index, but at a smaller level also in other directions in between, which is in agreement with the reports based on ion-range approaches for bulk materials [19].

**3.3.2. Channeling maps.** In the next step, both polar  $\Theta$  and azimuthal  $\phi$  angles were changed around selected low index directions, ( $0^\circ \leq \Theta \leq 30^\circ$ ) and ( $0^\circ \leq \phi \leq 130^\circ$ ) respectively. Considering the finite sizes of nanostructures, simulating higher polar angles would result in changes of the energy loss due to the geometry of the particle, as the ions at high polar angles would go through a smaller amount of matter. However, simulation of the entire azimuthal angles is doable but not necessary, as the map repeats itself after some points and one can exploit the intrinsic symmetries of the crystal as shown below. In order to get universal patterns, which are independent of the absolute ion energy-loss, the probability of losing energy at a given direction was

calculated and visualized in figure 8 which shows parts of the complete fcc channeling map centered around  $[001]$ ,  $[\bar{1}\bar{1}0]$  and  $[\bar{1}\bar{1}\bar{1}]$ .

The channeling map around  $[00\bar{1}]$ , presented in figure 8(a) has a mirror-image symmetry where the axis of symmetry locates at  $45^\circ$  of the  $[\bar{1}\bar{1}0]$  direction. This symmetrical behavior comes from the fcc  $\{001\}$  planes with an atomic arrangement of four-fold rotational symmetry and a mirror-image symmetry between each of the two high-symmetry rotational axes. The high-symmetry rotational angles are  $0^\circ/360^\circ$ ,  $90^\circ$ ,  $180^\circ$  and  $270^\circ$ , and the mirror-image symmetric counterparts are  $45^\circ$ ,  $135^\circ$ ,  $225^\circ$  and  $315^\circ$ . The channeling map around  $[\bar{1}\bar{1}0]$  shows a wide channel at an azimuthal angle of  $90^\circ$  (parallel to the  $(001)$  plane), covering around 10 azimuthal degrees. The channeling map around the  $[\bar{1}\bar{1}\bar{1}]$  direction shows a wide transparent region around  $20^\circ$ – $25^\circ$  polar angles. Notice that the wide bluish area is not one continuous channel along a particular fixed polar angle, but results from planar channel into the  $(1\bar{1}\bar{1})$  plane.

The  $\{111\}$  planes are the ABC stacked hexagonal layers with the six-fold rotational symmetry. Taking the BC stacking layers into account, the rotational symmetry becomes three-fold, with symmetrical axes at  $0^\circ/360^\circ$ ,  $120^\circ$  and  $240^\circ$ , figures 8(e), (f). There are also three mirror-image symmetries between each two rotational symmetrical axes, at azimuthal angles  $60^\circ$ ,  $180^\circ$  and  $300^\circ$ .

As stated earlier the origins of these channeling maps correspond to the three low index directions in the fcc system namely,  $[00\bar{1}]$ ,  $[\bar{1}\bar{1}0]$  and  $[\bar{1}\bar{1}\bar{1}]$ , respectively. Given that the incident polar angles are varied between  $0^\circ$  and  $30^\circ$  around each principal direction, none of these maps contains the neighboring principal directions. For instance: in the first channeling map where  $[00\bar{1}]$  is the origin, the  $[0\bar{1}\bar{1}]$  coordinate would be at  $(45^\circ, 45^\circ)$  = (polar, azimuthal) and  $[\bar{1}\bar{1}\bar{1}]$  would be at  $(55^\circ, 0^\circ)$ . Therefore all the channeling directions in these maps (bluish regions) are high-index directions between the principal ones. This clearly confirms the occurrence of ion channeling for nanostructured materials, not only in the principal directions, but also in the

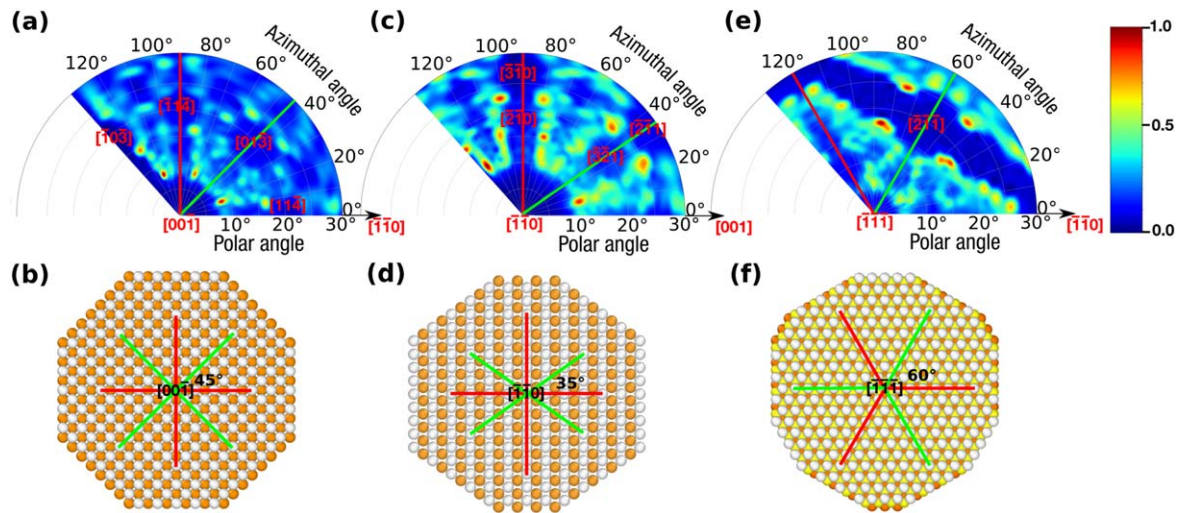


**Figure 8.** Channeling maps centered around the  $[00\bar{1}]$  (a),  $[\bar{1}\bar{1}0]$  (c), and  $[\bar{1}\bar{1}\bar{1}]$  (e) directions. The colors show the probability of losing energy by the ion. Red color corresponds to a high, deep blue to a low energy deposition. Correspondingly, the probability for the ion to channel is higher in the dark areas. (b), (d), (f) Atomic configurations illustrating the rotational symmetry and a mirror-image symmetry between each of the two high-symmetry rotational axes.

intermediate ones. This result is in agreement with reports on bulk materials. It also reflects the rather small amount of reconstructions of the surfaces in our simulations. From the results presented in figures 7 and 8 the well known result that the most transparent directions for fcc are in decreasing order the  $\langle 011 \rangle$  directions followed by  $\langle 001 \rangle$  and  $\langle 111 \rangle$ . This is not only visible in the small energy loss that ions experience in these directions but also from the width of the channels as can easily be seen by comparing figures 7(b) with (b).

This maps allow a qualitative interpretation of the strength and width of channeling directions through the color coding. In an experiment one can scan a small subset of polar and azimuthal angles (approx.  $\pm 20^\circ$ ) to obtain a subset of the presented channeling map. In a second step this can be uniquely identified in the pre-calculated map and the direction of the nanoparticle is determined [29, 31].

### 3.4. Effects of stacking faults

In order to address the general effects of defects on channeling, we considered stacking faults, as (i) they had lower energy and were much more stable than grain boundaries; (ii) had a well-defined structure, while many grain boundary structures are possible. Point and line defects like dislocations are unlikely in such small metal clusters due to a high mobility of vacancies and interstitials. Indeed our MD simulations of defects in 5 nm Au nanoclusters showed a higher stability of stacking faults, compared to other types of defects which easily can diffuse to the particle surface and annihilate there. To address the effects of stacking faults on channeling maps, He irradiation of 5 nm Au clusters containing intrinsic and extrinsic stacking faults, perpendicular to the  $[\bar{1}\bar{1}\bar{1}]$  plane, were simulated. The results are presented in figure 9. It is evident that planar defects give rise to partial blockage of the channels, yet the channeling/non-channeling

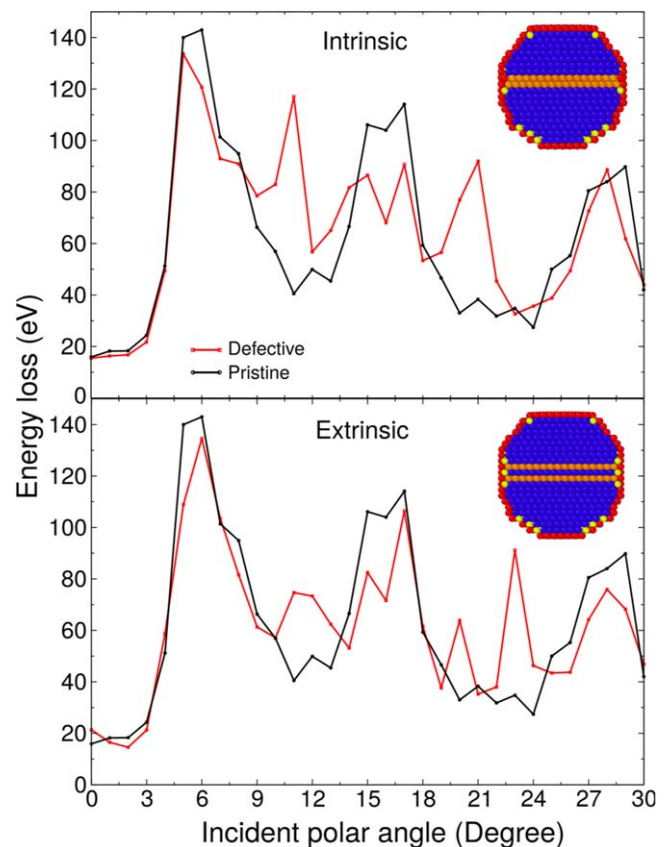


**Figure 9.** Channeling of He ions in gold nanoclusters with intrinsic and extrinsic faults. The faults are in the  $[111]$  plane, perpendicular to ion irradiation (for  $\Theta = 0$ ) direction. From plots it is evident that for an incident direction parallel to  $[\bar{1}\bar{1}\bar{1}]$  the selected stacking faults naturally do not have any effect on channeling. They do however, give rise to partial blockage of the channels at other angles. The polar angle is changed for a fixed azimuthal angle from  $[\bar{1}\bar{1}\bar{1}]$  towards  $[1\bar{1}0]$  around  $[\bar{1}\bar{1}2]$ .

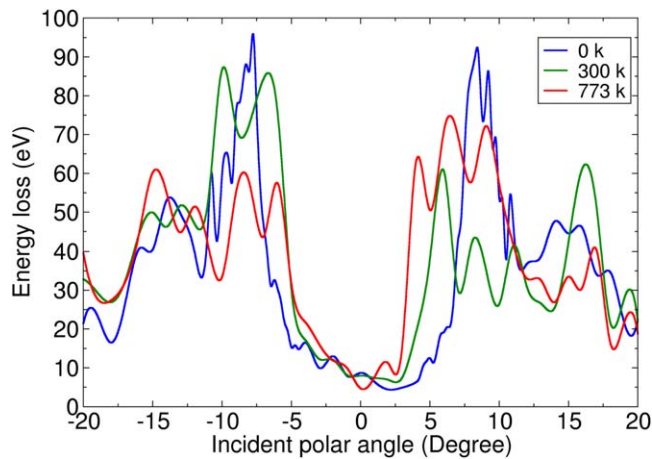


**Figure 10.** Energy loss at different temperatures. Overall weak effect of temperature on channeling maps is evident. The ion beam direction is along  $[00\bar{1}]$  into a cluster with 5 nm diameter. Incident azimuthal angle is fixed ( $[00\bar{1}]$  towards  $[\bar{1}\bar{1}\bar{1}]$ ).

directions are preserved. This indicates that the intrinsic symmetries are not fully broken. On the other hand, the signatures of stacking faults can be identified in the channeling maps through the comparison of the maps of pristine and defective clusters. As expected the additional atoms in the center of the channel lead to an increase of the energy loss in the middle of the channel. For the selected geometry, presented in figure 9, this happens for directions other than  $\langle 111 \rangle$  as is evident from the plots. In the presented case an additional dechanneling peak occurs in the middle of the  $[\bar{3}\bar{5}\bar{4}]$  and the  $[\bar{1}\bar{3}\bar{2}]$  directions. In the past dechanneling due to stacking faults has been observed in the HIM for channeling along the  $[\bar{1}\bar{1}0]$  direction induced by a local change from fcc to hcp stacking for 2 ML Ag on Pt(111) [32].

### 3.5. Effects of temperature

Finally, we studied the effects of finite temperatures on channeling. The velocities of atoms in the cluster were equilibrated to match the desired temperature, then MD simulation of He ion impacts were carried out using the same setup as for zero temperature simulations. The results are presented in figure 10.

It is evident that temperature has an overall weak effect on channeling, as the channeling/non-channeling directions remain the same. Nevertheless, temperature does change the channel widths, which is an intuitive result: the higher the temperature, the more the atoms vibrate increasing the chances for an impinging-ion/target-atom collision, resulting in narrower channels. This can be seen from the plots in figure 10 in which the width of the  $[00\bar{1}]$  channel is reduced from nearly  $\Psi_{1/2} = 6^\circ$  to roughly  $\Psi_{1/2} = 3.5^\circ$ .

### 3.6. Size-dependent properties

As system size is an important factor for nanostructured materials, we also investigated size dependence of the studied properties. For this purpose, 30 keV He irradiation of gold

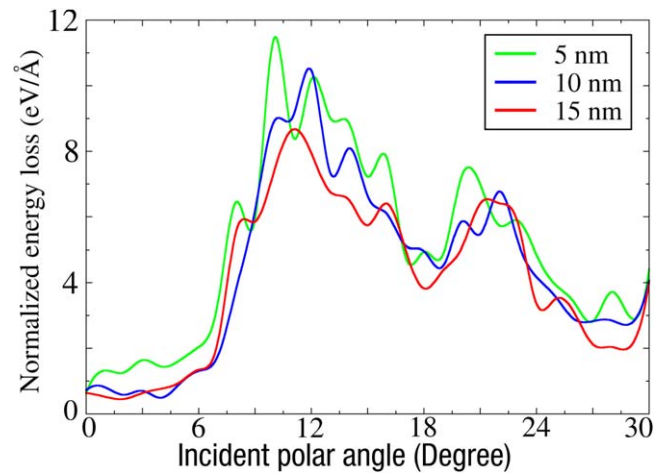


**Figure 11.** Energy loss of 30 keV He ions in Au clusters with diameters of 5, 10, and 15 nm. Energy loss is normalized by cluster diameter. The ion beam direction is parallel to  $[0\bar{1}\bar{1}]$ . The incident azimuthal angle is fixed ( $[0\bar{1}\bar{1}]$  towards  $[0\bar{1}0]$ ).

nanoclusters with larger diameters of 10 and 15 nm were simulated and compared to the results for the smaller target.

**3.6.1. Ion energy-loss.** Figure 11 presents the calculated energy loss of 30 keV He ions impinging the  $\{110\}$  surface for all the clusters we studied. The energy loss was normalized according to the total length the ion travels, that is cluster diameter. It is evident that Au nanoclusters of different sizes show a similar ion energy loss pattern, revealing that these patterns originate from the intrinsic symmetries of the corresponding crystalline configurations and they share common channeling/non-channeling directions. However, a more careful look reveals that by comparing the largest cluster with the smallest cluster one can see that some of the fine structure is lost for the bigger cluster. This finite size effect is related to the fact that very small high Miller index channels become too narrow for transmission with increasing channel length.

**3.6.2. Sputtering yield.** As the cluster size increases, its surface-to-volume ratio drops, thus a lower sputtering-yield is expected. Our results fulfill this expectation, as is evident from figure 12 where the sputter yield for two different cluster sizes is presented. Nevertheless the dependence of the sputter yield on the incident angle is size-independent. It was reported earlier [54] that for Pt cluster with sizes of 2–5 nm under 3 keV He ion irradiation the sputter yield does not depend on the cluster size, but our results show a size-dependent sputtering yield for 5–10 nm size ranges, which is associated with an order of magnitude higher ion energy. For the used energy of 30 keV the collision cascade significantly exceeds the size of the nanoparticle and size depend forward sputtering becomes an effective process.

**3.6.3. Channeling maps.** A channeling map for a 10 nm cluster is presented in figure 13, where zero angles correspond to the ion beam direction perpendicular to the  $\{100\}$

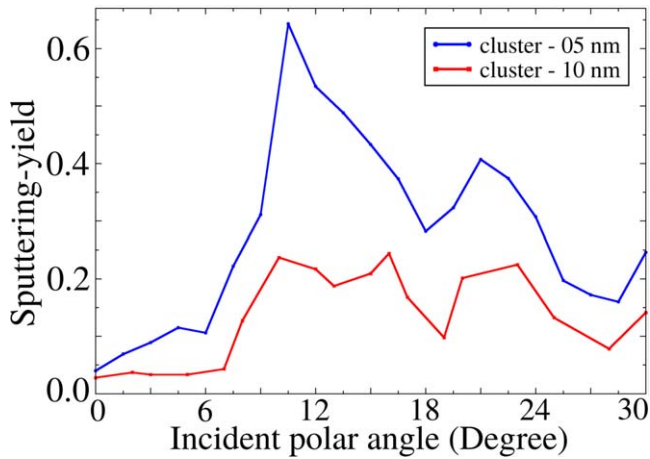


**Figure 12.** A comparison between the sputter yield from clusters with sizes of 5 and 10 nm. The irradiation geometry covers  $30^\circ$  polar angle measured from  $[0\bar{1}\bar{1}]$  towards  $[0\bar{1}0]$  around  $[\bar{1}00]$ .

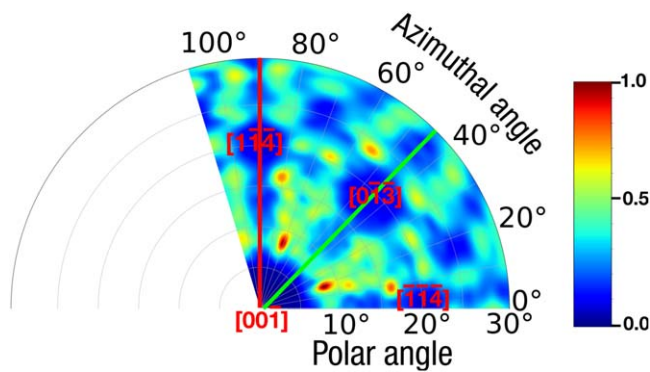


**Figure 13.** Channelling map around  $[00\bar{1}]$  for a gold cluster with a diameter of 10 nm. The colors show the probability of losing energy by the ion.

direction. It is similar to those obtained for the small cluster, figure 8(a). As evident from our simulations, channelling maps and sputtering patterns of Au clusters are independent of the system sizes and show a universal behavior. Therefore, one can expect that the overall patterns of bigger clusters are the same. As already observed in figures 11 and 12 the larger cluster size leads to a loss of fine structure, which is expected from simple transparency arguments. For the very small cluster some high Miller index channels will result in anomalous high transmission yields and low energy losses due to their finite length.

#### 4. Discussions and conclusions

While analytic solutions exist for high energy channeling into bulk samples [53] (i.e. where the dimension along the beam direction is much larger than the range of the penetrating ions) they cannot be applied without further changes to low energy channeling into nano-objects. The reasons are mainly that (I) some of the assumptions and simplifications are not valid at low energies and that (II) it is required to evaluate

backscattering yields and dechanneling probabilities. Both of these quantities cannot easily be measured in a FIB or HIM. However, it has been shown that channeling and blocking related effects are not only observable, but can also be used to obtain quantitative information on the sample structure [29, 31, 32]. In view of current efforts to develop new transmission based imaging modes in the HIM [55, 56] it is necessary to investigate the behavior of nano-scale structures. Special attention should be given to the obtainable signals as well as the stability of the nanostructures. However, for very small sample dimensions along the beam direction the following questions have to be answered:

- (i) Does the transmitted signal carry sufficient information?
- (ii) Will the unavoidable damage hinder the collection of sufficiently high signal to noise ratio?
- (iii) Which imaging modes are feasible?

The presented simulations clearly show that besides classical bright field/dark field imaging more sophisticated imaging modes are possible. The first two points from the above list have already been answered positively in experiments on large membranes. With respect to the last point, so far only channeling has been demonstrated in transmission mode imaging of thin membranes but not for nanoparticles. From our simulations, it becomes clear that not only can channeling be observed for small gold clusters down to 5 nm diameter, but the clusters can also survive the irradiation with a highly FIB. The induced energy can easily be dissipated away from the nanoparticle and only sputtering will limit the possible exposure. However, direct knock-on related sputtering is weak for helium in the investigated energy range [57]. Our simulations also show that the directional dependency of the ion energy loss can be used for obtaining information on the internal structure of nanoparticles. In the light of the recent development of imaging modes that rely on the high-speed blanking of the primary ion beam to obtain time-of-flight spectra [58, 59] ion energy loss spectroscopy becomes also possible. It is appropriate at this point to draw attention to the fact that our calculations ignore the effects of the anisotropy of the electron density on the electronic stopping. In a first approximation one can assume that, as long as the cross sections for electronic stopping of the individual atoms do not strongly overlap, the energy loss related to electronic stopping qualitatively behaves in a similar way as the nuclear stopping. This argument is similar to what has been used to understand the channelling related changes in x-ray emission from metals and organic-crystals [60, 61]. In practice the qualitative change in the total ion energy loss will behave like the ion energy loss related to nuclear stopping alone and the above results can be utilized to understand the internal structure of the nanoparticles. In the past attempts have been made to include electronic stopping in MD calculations [62] using the Oen-Robinson [63] inelastic energy loss function. While this is a possible approach it does not result in qualitatively new insights, and goes beyond the current more fundamental work presented here.

In the last part of the work we also looked at the effect of stable planar defects inside the nanoparticles. The found changes in the directional dependence of the ion energy loss if a stacking fault is placed inside the channel is not different from what is known from RBS/channeling [16, 64]. However, HIM has demonstrated that it is able to pick up the associated minute changes of the atomic positions in channeling [32]. Provided a sensitive enough detector can be made available in the HIM we expect the method to be able to reveal stacking faults as well as surface reconstructions in transmission mode.

To sum up, we performed MD simulations of 30 keV He ion impacts onto Au clusters with diameters of 5–15 nm. We showed that impacts of the ions can give rise to substantial heating of the clusters through deposition of energy into electronic degrees of freedom, but it does not affect channeling, as the clusters cool down between consecutive impact of the ions under typical imaging conditions. At the same time, high temperatures and small sizes should give rise to fast annealing of defects so that the system remains crystalline. Our results show that ion-channeling occurs not only in the principal low-index, but also in the intermediate directions. The strengths of different channels are specified, and their correlations with sputtering-yield and damage production is discussed. The effects of stacking faults on channeling were also addressed. Furthermore, the size-dependence of these properties was studied, and a universal behavior was found. Overall, our results make it possible to understand the behavior of Au clusters under irradiation in HIM and facilitate the interpretation of HIM images with account for structural changes, energy deposition and associated heating, as well as channeling effects.

## Acknowledgments

The atomic visualizations are created using the Open Visualization Tool (OVITO) [48]. Nanoparticles are generated using Wulff construction method implemented in Virtual NanoLab (VNL) [65]. The computational support from the HZDR computing cluster is gratefully appreciated. This work is part of the npSCOPE project and has received funding from the European Union's Horizon 2020 research and innovation programme. Grant Number: 720964.

## ORCID iDs

Sadegh Ghaderzadeh  <https://orcid.org/0000-0003-4416-7147>

Mahdi Ghorbani-Asl  <https://orcid.org/0000-0003-3060-4369>

Silvan Kretschmer  <https://orcid.org/0000-0002-5098-5763>

Gregor Hlawacek  <https://orcid.org/0000-0001-7192-716X>

Arkady V Krasheninnikov  <https://orcid.org/0000-0003-0074-7588>

## References

- [1] Reed M, Randall J, Aggarwal R, Matyi R, Moore T and Wetsel A 1988 *Phys. Rev. Lett.* **60** 535
- [2] Wilcoxon J and Abrams B 2006 *Chem. Soc. Rev.* **35** 1162–94
- [3] Miura M et al 2017 *NPG Asia Mater.* **9** e447
- [4] Jin R, Zeng C, Zhou M and Chen Y 2016 *Chem. Rev.* **116** 10346–413
- [5] Krasheninnikov A and Banhart F 2007 *Nat. Mater.* **6** 723–33
- [6] Krasheninnikov A and Nordlund K 2010 *J. Appl. Phys.* **107** 3
- [7] Dhara S 2007 *Crit. Rev. Solid State Mater. Sci.* **32** 1–50
- [8] Lehtinen O, Kotakoski J, Krasheninnikov A, Tolvanen A, Nordlund K and Keinonen J 2010 *Phys. Rev. B* **81** 153401
- [9] Ghorbani-Asl M, Kretschmer S, Spearot D and Krasheninnikov A 2017 *2D Mater.* **4** 025078
- [10] Kalbac M, Lehtinen O, Krasheninnikov A and Keinonen J 2013 *Adv. Mater.* **25** 1004–9
- [11] Nietiadi M, Sandoval L, Urbassek H and Möller W 2014 *Phys. Rev. B* **90** 045417
- [12] Greer J, Oliver W and Nix W 2005 *Acta Mater.* **53** 1821–30
- [13] Jadwiszczak J et al 2018 arXiv:1811.09545
- [14] Nanda G, Hlawacek G, Goswami S, Watanabe K, Taniguchi T and Alkemade P 2017 *Carbon* **119** 419–25
- [15] Nastasi M, Mayer J and Wang Y 2014 *Ion Beam Analysis: Fundamentals and Applications* (Boca Raton, FL: CRC Press)
- [16] Feldman L, Mayer J and Picraux S 1982 *Materials Analysis by Ion Channeling: Submicron Crystallography* (New York: Academic)
- [17] Feldman L, Mayer J and Picraux S 2012 *Materials Analysis by Ion Channeling: Submicron Crystallography* (New York: Academic)
- [18] Nordlund K and Hobler G 2018 *Nucl. Instrum. Methods Phys. Res. B* **435** 61–9
- [19] Nordlund K, Djurabekova F and Hobler G 2016 *Phys. Rev. B* **94** 214109
- [20] Hlawacek G and Götzhäuser A 2016 *Helium Ion Microscopy* (Berlin: Springer)
- [21] Hlawacek G, Veligura V, van Gastel R and Poelsema B 2014 *J. Vac. Sci. Technol. B* **32** 020801
- [22] Veligura V, Hlawacek G, van Gastel R, Zandvliet H and Poelsema B 2012 *Beilstein J. Nanotechnol.* **3** 501
- [23] Boverhof D and David R 2010 *Anal. Bioanal. Chem.* **396** 953–61
- [24] Pietroiusti A, Magrini A and Campagnolo L 2016 *Toxicol. Appl. Pharmacol.* **299** 90–5
- [25] Ward B, Notte J and Economou N 2006 *J. Vac. Sci. Technol. B* **24** 2871–4
- [26] Fox D and Zhang H 2018 *Helium ion microscopy Progress in Nanoscale Characterization and Manipulation* (Berlin: Springer) pp 479–508
- [27] Maas D and van Gastel R 2013 *Helium ion microscopy Surface Science Techniques* (Berlin: Springer) pp 461–97
- [28] Franklin R, Kirk E, Cleaver J and Ahmed H 1988 *J. Mater. Sci. Lett.* **7** 39–41
- [29] Veligura V, Hlawacek G, van Gastel R, Zandvliet H and Poelsema B 2012 *Beilstein J. Nanotechnol.* **3** 501–6
- [30] Hlawacek G, Veligura V, Lorbek S, Mocking T, George A, van Gastel R, Zandvliet H and Poelsema B 2012 *Beilstein J. Nanotechnol.* **3** 507–12
- [31] Langlois C, Douillard T, Yuan H, Blanchard N, Descamps-Mandine A, Van de Moortèle B, Rigotti C and Epicier T 2015 *Ultramicroscopy* **157** 65–72
- [32] Hlawacek G, Jankowski M, Wormeester H, van Gastel R, Zandvliet H and Poelsema B 2016 *Ultramicroscopy* **162** 17–24
- [33] Zhurkin E 2009 *J. Surf. Invest. X-ray, Synchrotron Neutron Tech.* **3** 192–8

- [34] Järvi T and Nordlund K 2012 *Nucl. Instrum. Methods Phys. Res. B* **272** 66–9
- [35] Kissel R and Urbassek H 2001 *Nucl. Instrum. Methods Phys. Res. B* **180** 293–8
- [36] Zimmermann S and Urbassek H 2008 *Int. J. Mass Spectrom.* **272** 91–7
- [37] Järvi T, Pakarinen J, Kuronen A and Nordlund K 2008 *Europhys. Lett.* **82** 26002
- [38] Zhurkin E 2008 *J. Surf. Invest. X-ray, Synchrotron Neutron Tech.* **2** 193–9
- [39] Ohya K 2018 *AIP Adv.* **8** 015120
- [40] Fassbender J, Ravelosona D and Samson Y 2004 *J. Phys. D: Appl. Phys.* **37** R179
- [41] Chappert C et al 1998 *Science* **280** 1919–22
- [42] Mangeney J, Choumane H, Patriarche G, Leroux G, Aubin G, Harmand J, Oudar J and Bernas H 2001 *Appl. Phys. Lett.* **79** 2722–4
- [43] Björkas C, Nordlund K, Arstila K, Keinonen J, Dhaka V and Pessa M 2006 *J. Appl. Phys.* **100** 053516
- [44] Dhaka V et al 2006 *Semicond. Sci. Technol.* **21** 661
- [45] Plimpton S 1995 *J. Comput. Phys.* **117** 1–19
- [46] Ackland G, Tichy G, Vitek V and Finnis M 1987 *Phil. Mag. A* **56** 735–56
- [47] Ziegler J and Biersack J 1985 *The Stopping and Range of Ions in Matter* (Boston, MA: Springer) pp 93–129
- [48] Stukowski A 2009 *Modell. Simul. Mater. Sci. Eng.* **18** 015012
- [49] Sun L, Krasheninnikov A, Ahlgren T, Nordlund K and Banhart F 2008 *Phys. Rev. Lett.* **101** 156101
- [50] Ziegler J, Ziegler M and Biersack J 2010 *Nucl. Instrum. Methods Phys. Res. B* **268** 1818–23
- [51] Schmid G and Corain B 2003 *Eur. J. Inorg. Chem.* **2003** 3081–98
- [52] Green B, Budy S, Reed S and Siemens M 2018 *J. Appl. Phys.* **124** 144301
- [53] Lindhard J 1965 *Influence of Crystal Lattice on Motion of Energetic Charged Particles* vol 34 (Copenhagen: Munksgaard)
- [54] Järvi T, Kuronen A, Nordlund K and Albe K 2009 *Phys. Rev. B* **80** 132101
- [55] Kavanagh K, Herrmann C and Notte J 2017 *J. Vac. Sci. Technol. B* **35** 06G902
- [56] Wang J, Huang S, Herrmann C, Scott S, Schiettekatte F and Kavanagh K 2018 *J. Vac. Sci. Technol. B* **36** 021203
- [57] Kretschmer S, Maslov M, Ghaderzadeh S, Ghorbani-Asl M, Hlawacek G and Krasheninnikov A 2018 *ACS Appl. Mater. Interfaces* **10** 30827–36
- [58] Klingner N, Heller R, Hlawacek G, von Borany J, Notte J, Huang J and Facsko S 2016 *Ultramicroscopy* **162** 91–7
- [59] Klingner N, Heller R, Hlawacek G, Facsko S and von Borany J 2019 *Ultramicroscopy* **198** 10–7
- [60] Brandt W, Khan J, Potter D, Worley R and Smith H 1965 *Phys. Rev. Lett.* **14** 42–4
- [61] Brandt W, Dobrin R, Jack H Jr, Laubert R and Roth S 1968 *Can. J. Phys.* **46** 537–42
- [62] Karolewski M and Cavell R 2011 *Surf. Sci.* **605** 1842–51
- [63] Oen O and Robinson M 1976 *Nucl. Instrum. Methods* **132** 647–53
- [64] Feldman L 2006 *Phys. Scr.* **28** 303–7
- [65] Schneider J, Hamaekers J, Chill S, Smidstrup S, Bulin J, Thesen R, Blom A and Stokbro K 2017 *Modelling Simul. Mater. Sci. Eng.* **25** 085007